Signal, Image and Video Processing (2019) 13:813–821
https://doi.org/10.1007/s11760-019-01417-4

ORIGINAL PAPER

Sampling with level set for pigmented skin lesion segmentation

Tiejun Yang[1] · Yaowen Chen[1] · Jiewei Lu[1] · Zhun Fan[1]

Received: 20 July 2018 / Revised: 27 November 2018 / Accepted: 3 January 2019 / Published online: 12 January 2019

Abstract
Melanoma is the deadliest form of skin cancer, and its incidence is increasing. The first step in automated melanoma analysis of dermoscopy images is to segment the area of the lesion from the surrounding skin. To improve the accuracy and adaptability of segmentation, an algorithm called sampling with level set by integrating color and texture (SLS-CT) is proposed that not only designs a new way to incorporate textural and color features in the definition of the energy functional but also utilizes an index called texture level, proposed in this work, to automatically decide the weight of each feature in the combined energies. First, at the preprocessing stage, hair and black frame removal is applied, and a potential lesion area is then obtained using Otsu thresholding and entropy maximization. Thereafter, the probability distribution of prior color in this potential lesion area is calculated as well. Second, Gabor wavelet-based texture features are extracted and integrated with the prior color into the evolving energies of the level set based on the texture level. To achieve global optimization, a Markov chain Monte Carlo sampling approach guided by the combined energy is adopted in evolving the level set, which ultimately defines a border in the image to segment a lesion from normal skin. Finally, morphological operations are used for postprocessing. The experimental results of the proposed algorithm are compared with those of other state-of-the-art algorithms, demonstrating that the proposed algorithm outperforms the other tested ones in terms of accuracy and adaptability to different databases.

Keywords Pigmented skin lesion · Level set · Texture · Markov chain Monte Carlo · Image segmentation

1 Introduction

Malignant melanoma is the deadliest form of skin cancer, and the number of invasive melanoma cases is increasing rapidly. In fact, early-stage melanoma can be cured with a simple excision. Melanoma screenings such as skin self-examination or total body skin examination are recommended for early detection. However, the interpretation of such examinations is time-consuming and subjective, even for trained dermatologists. Therefore, the development of computer-aided diagnostic techniques for automatic or semiautomatic diagnosis of skin lesions is essential for facilitating early diagnosis of malignant melanoma [1, 2].

Accurate segmentation facilitates clinical quantitative analysis. In recent decades, many segmentation algorithms have been proposed to detect the borders of pigmented skin lesions either automatically or semiautomatically [3–6]. These algorithms can be classified into the following categories: thresholding, edge-based, clustering [7, 8], region-based, active contours [9–12] and supervised learning, among others. The thresholding and edge-based methods both encounter problems when the modes of the two regions overlap or when the transition between them is vague, e.g., blurred lesion borders or low contrast between the lesion and surrounding skin. To address these problems, region-based methods such as clustering and region merging have been proposed.

To select more features automatically and integrate more prior knowledge, supervised learning methods are widely used in medical image segmentation [13, 14]. Roth et al. [15] proposed DeepOrgan, a method of pancreas segmentation using convolutional neural networks (CNNs). This method first uses random forest (RF) to generate region proposals (RPs) and then employs several CNNs to classify RPs from coarse to fine. In a previous work [16], a method of pigmented skin lesion segmentation based on RF is proposed. First, RPs are generated by statistical region merging (SRM). Then, Gabor wavelet transform-based texture and red (R), green (G), blue (B) color features of RPs are combined and

✉ Zhun Fan
zfan@stu.edu.cn

[1] Guangdong Provincial Key Laboratory of Digital Signal and Image Processing Techniques, Department of Electrical Engineering, Shantou University, Guangdong, People's Republic of China

fed into RF for training and testing. This kind of RP classification method has the deficiency of heavy dependence on RPs, i.e., if RPs are not generated accurately, the classification accuracy may not be satisfactory. Without the generation of RPs, Jafari et al. [17] made preprocessed patches of input images and fed them into a convolutional neural network for training and testing. However, one shortcoming of supervised learning is that a large and accurate training dataset is usually required. Especially for medical image analysis, it is very difficult to obtain such a dataset.

Active contour [18] is another well-known segmentation model that is capable of integrating local and global features, such as gradients, curvature and mean intensity. Silveira et al. [19] compared four methods of active contour (two with snakes and two with level set) in pigmented skin lesion segmentation: gradient-based gradient vector flow (GVF) snakes [20], active snakes using expectation maximization (EM) [21], regional color based on Chan and Vese's level set (CV) [22] and an extension of CV combined with EM (EM-CV) [19]. These four methods directly use pixel colors or features derived from them to drive the explicit curves (snakes) or the implicit curves embedded in a high-dimensional space (level set). However, none of them has considered integration of texture feature.

Ma and Tavares [23] presented a semiautomatic method based on a level set to handle the segmentation of skin lesions in dermoscopic images. The method uses the contrasts between the lightness and saturation of the skin lesions and the surrounding normal skin to build the driving energies. However, the initial curve needs to be defined manually to cover the entire region of the skin lesion to ensure that the initial curve will then move inward until it arrives at the boundaries of a skin lesion. The estimated distributions of the lightness and saturation also depend on the initial curve.

The most similar method to ours is the one called Markov chain Monte Carlo sampling with level set (MCMC-LS) [24]. MCMC-LS is an efficient, globally optimized level set segmentation method in which each iteration of the evolving level set is sampled using Metropolis–Hastings MCMC sampling. MCMC-LS introduces a perturbation based on intensity and internal constraint energies, leading to the proposal of evolving level sets being accepted more properly and efficiently.

Unfortunately, the work performed in [24] did not include a discussion of texture integration and determination of the relative importance of different energies. In fact, in addition to intensity and color, a pigmented skin lesion usually has some unique texture features not observed in normal skin, hair and vessels [25]. Therefore, texture features are suitable for integration with color in pigmented skin lesion segmentation. Furthermore, because melanoma regions are more textured than nonmelanoma regions, the relative importance of energies based on color or texture is not equal in segmentation. Thus, it is necessary to differentiate the importance of energies during level set segmentation for differently textured skin lesions, according to texture level (TL), as proposed in this work.

In this paper, we propose a level set-based segmentation method for pigmented skin lesion in dermoscopy images to achieve the following two objectives: (1) to improve the accuracy of segmentation by integrating additional microfeatures such as textures, which we believe is an issue not sufficiently discussed in pigmented skin lesion segmentation [26], and (2) to improve adaptability by distinguishing the importance of features in response to different inner textures. In our method, TL is introduced to facilitate the adaptable integration of energies based on color and texture. In addition, Gabor wavelet transform is used to extract different orientations and scales of texture features, which are added into a variational level set segmentation model. Moreover, to obtain global optimization, MCMC sampling is adopted in evolving the level set.

Some preprocessing methods, including black frame removal and approximate lesion localization [27], are also introduced to further improve the performance of the algorithm.

The remainder of this paper is organized as follows. In Sect. 2, the proposed algorithm is explained in detail. In Sect. 3, the experimental results and a discussion are presented. Finally, the conclusions are provided in Sect. 4.

2 Methods

Our method, named sampling with level set by integrating color and texture (SLS-CT), comprises three major stages: preprocessing, segmentation and postprocessing. (Details of the algorithm are shown in Fig. 1.) In the stage of preprocessing, we use a tool called DullRazor [28] to remove hair, if present, and use a method based on clustering to remove black frames in dermoscopy images. Subsequently, a method of approximate lesion localization based on the maximum entropy principle (MEP) is used, and the preprocessed result is fed into the subsequent stage of segmentation. The details of this stage are described in Sect. 2.1. In the next stage of segmentation, we build a prior color energy based on the result of approximate lesion localization and a texture energy based on Gabor wavelet transform. Then, we integrate these energies using a novel index named *texture level* to guide sampling based on MCMC-LS. These details are described in Sects. 2.2. Finally, in the postprocessing stage, mathematical morphology operations are used to erase tiny islands and fill in small holes in Sect. 2.3.

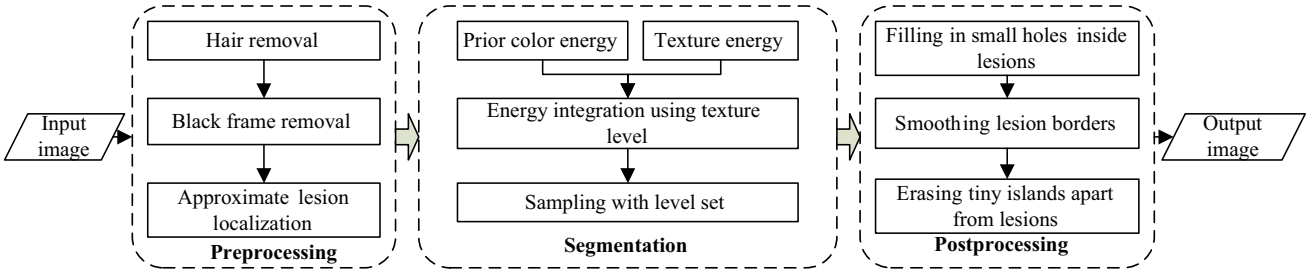

Fig. 1 Flowchart of SLS-CT, including preprocessing, segmentation and postprocessing steps

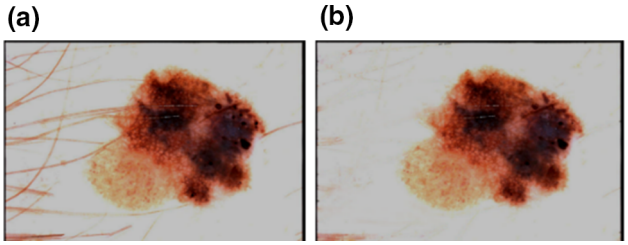

Fig. 2 An illustrative example of hair removal using DullRazor: **a** the original image; **b** the image after hair removal

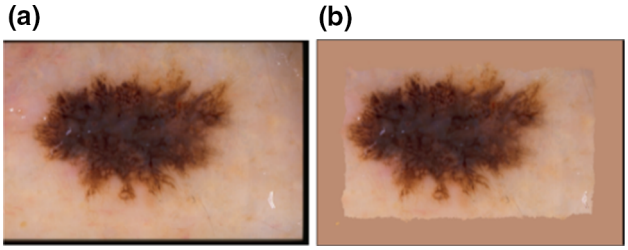

Fig. 3 An example of black frame removal: **a** the original image; **b** removal results for the rectangular black frames

2.1 Preprocessing

Here, we use three steps of preprocessing, namely hair removal, black frame removal and approximate lesion localization. Hair and black frame removal is employed to erase irrelevant objects, and the aim of approximate lesion localization is to roughly locate lesions.

2.1.1 Hair and black frame removal

A tool named DullRazor [28] is directly used to remove any hair present in a dermoscopic image. An illustrative example of hair removal is illustrated in Fig. 2.

Black frames usually exist in dermoscopic images due to unsatisfactory illumination conditions. Here, we used a method based on k-means clustering [29] to remove black frames. An example of black frame removal is depicted in Fig. 3. The detailed descriptions of black frame removal are as follows:

(a) Given an image $f(i,j)$ with spatial resolution $M*N$, convert it from RGB color space to CIE $L*a*b*$ color space.
(b) Choose the $a*$ and $b*$ channels as two components of the vector features for k-means clustering.
(c) Build the third component, d, of the vector features by the method given below:

$$d(i,j) = \begin{cases} -\left[\min\left(\frac{M}{2} - \left|i - \frac{M}{2}\right|, \frac{N}{2} - \left|j - \frac{N}{2}\right|\right)\right]^{n_1}, \\ \text{if black frames are rectangular.} \\ \left[\sqrt{\left(i - \frac{M}{2}\right)^2 + \left(j - \frac{N}{2}\right)^2}\right]^{n_1}, \\ \text{if black frames are circular.} \end{cases} \tag{1}$$

where n_1 is a constant to adjust the area of the black frames. The values of d for black frames are always greater than those for lesions.

(d) Classify the vector features into three classes in '$a*b* + d$' space using k-means clustering, where '+' means addition of two vectors in the vector space.
(e) Label each class as black frame, normal skin or skin lesion according to the following relationship:

$$\bar{d}_b > \bar{d}_s > \bar{d}_l \tag{2}$$

where $\bar{d}_b$, $\bar{d}_s$ and $\bar{d}_l$ are the mean values of d defined by Eq. (1) for the classes black frame, normal skin and skin lesion, respectively.

(f) Replace the color of the black frame class with the mean color of the normal skin class.

Some illustrative examples of removal results are shown in Fig. 3b. Note that we extract color features in CIE $L*a*b*$ color space instead of RGB because color differences are

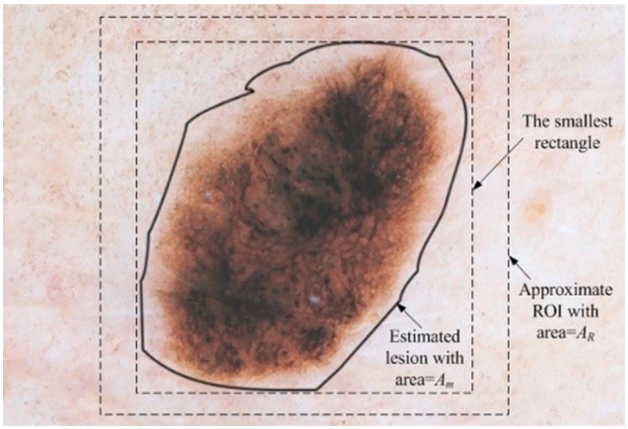

Fig. 4 Approximate lesion localization based on Otsu thresholding segmentation and entropy maximization

more distinguishable in the former color space [30] for the three classes.

2.1.2 Approximate lesion localization

The preprocessing stage also includes a method for approximate lesion localization. Inspired by the method of automatic color channel selection proposed in [19], which uses MEP to determine which color channel to choose, we developed a technique for approximating the ROI location using Otsu thresholding based on MEP.

Assume a given image contains an obvious area of pigmented skin lesion. The entropy of the approximate ROI is maximized only if the area of the ROI satisfies the following equation:

$$A_{\mathrm{R}} = 2A_{\mathrm{m}}, \tag{3}$$

where A_{m} is the estimated lesion area segmented by Otsu thresholding and A_{R} is the area of the ROI, which has the same centroid as the smallest rectangle containing the estimated lesion (as shown in Fig. 4).

The details of approximate lesion localization are given below:

(a) Use Otsu thresholding to segment the input image into a binary image, f_{Otsu}, based on its blue channel in RGB color space. Note that the blue channel is selected because it best facilitates discrimination of lesions from normal skin [31].
(b) With the given f_{Otsu}, find the smallest rectangle to encompass the skin lesion area.
(c) Based on the smallest rectangle, crop the input image into a smaller rectangular one with a proper size to fulfill the condition in Eq. (3), as shown in Fig. 4.

2.2 Segmentation

First, an energy functional is constructed based on prior color and texture. Then, TL is introduced to decide the weights of the integrated energies adaptively. Finally, MCMC sampling is adopted to obtain global optimization.

2.2.1 Prior color energy

During approximate lesion localization, we used Otsu thresholding to estimate the area of a lesion based on color. Thus, the estimated result, f_{Otsu}, is reused to calculate the estimated probability $p(x, y)_{\mathrm{K(clr)}}$ of each pixel belonging to the lesion or the background. The energy of the prior color [32], $E_{\mathrm{K(clr)}}$, is given by

$$\begin{cases} E_{K(\mathrm{clr})} = -\log\big(p(x,y)_{K(\mathrm{clr})} + \varepsilon\big), \\ p(x,y)_{K(\mathrm{clr})} = \begin{cases} 1, \text{ if } f_{\mathrm{Otsu}}(x,y) = 0 \\ 0, \text{ if } f_{\mathrm{Otsu}}(x,y) = 1 \end{cases} \end{cases} \tag{4}$$

where ε is an additive tiny positive constant in case $p(x, y)_{K(\mathrm{clr})} = 0$. Notably, we use prior color instead of color to build the energy because color is unreliable, especially when lesions have varied coloring. Prior color provides an estimation of color information of lesions, which can be further refined by other features.

2.2.2 Texture energy

To improve the accuracy of segmentation by integrating additional microfeatures, we use Gabor wavelet transform to extract texture features, which has been a very useful tool in texture analysis in our previous work [16] and An's work [33]. Because Gabor wavelet transform is not sensitive to illumination variations and a certain degree of geometric transformation, we use this method to extract the texture features of the skin and lesion, which are defined by

$$\begin{cases} w(u,v) = \iint f(x,y) h_{\mathrm{G}}^{*}(u-x, v-y)\mathrm{d}x\mathrm{d}y, \\ h_{\mathrm{G}}(x,y|\sigma,u,v) = \\ \dfrac{1}{2\pi\sigma^2}\exp\left(-\dfrac{x^2+y^2}{2\sigma^2}\right)\exp[-j2\pi(ux+vy)], \end{cases} \tag{5}$$

where (u, v) is a spatial frequency, $h_{\mathrm{G}}(\cdot)$ is the Gabor wavelet function [34], σ is the standard deviation, * is a complex conjugate operator and $w(\cdot)$ is the coefficient of Gabor wavelet transform.

Let S and K be the total number of the scale and direction of $h_{\mathrm{G}}(\cdot)$, respectively. $S \times K$ wavelet transforms of an image will yield $S \times K$ results of wavelet coefficients, denoted by $w_{s,k}$, $s = 0, 1, \ldots S-1$, $k = 0, 1, \ldots K-1$.

To transform the Gabor texture feature into a probabilistic feature, kernel density estimation (KDE) is used, which is given by

$$\begin{cases} p_{\text{tex.obj}} = \hat{p}_h(w(u,v)|\phi(u,v) \geq 0), \\ p_{\text{tex.bkg}} = \hat{p}_h(w(u,v)|\phi(u,v) < 0), \\ \hat{p}_h(w) = \frac{1}{nh}\sum_{i=1}^{n} K_h(w, w_i), \\ K_h(w, w_i) = \frac{1}{\sqrt{2\pi}} e^{-\frac{1}{2}\left(\frac{w, w_i}{h}\right)^2} \end{cases} \tag{6}$$

where $p_{\text{tex.obj}}$ and $p_{\text{tex.bkg}}$ represent the probability distributions of the texture features of the object (lesion) and the background, respectively, ϕ is the level set function, $K_h(\cdot)$ is the Gaussian kernel function with the bandwidth h and n is the number of pixels in the given image.

Using Eq. (6), the texture feature is transformed to a probabilistic feature and can be integrated into the energy functional. Here, we adopt Jensen–Shannon divergence (JSD) [35] for the integration, which is defined by

$$\begin{cases} \text{JSD}(P\|Q) = \frac{1}{2}D(P\|M) + \frac{1}{2}D(Q\|M), \\ M = \frac{1}{2}(P+Q), \end{cases} \tag{7}$$

where P and Q are two probability distributions to be measured, $\text{JSD}(\cdot\|\cdot)$ is the similarity between P and Q. $D(\cdot\|\cdot)$ is the Kullback–Leibler divergence (KLD) [36], which is given by

$$D(P\|Q) = \sum_i P(i) \log\left(P(i)/Q(i)\right). \tag{8}$$

Then, the energy of texture $E_{f(\text{tex})}$ can be written as

$$E_{f(\text{tex})} = \text{JSD}\left(p_{\text{tex.obj}} \| p_{\text{tex.bkg}}\right). \tag{9}$$

Now the proposed energy functional $E(\phi; f)$ is given as

$$E(\phi; f, K_{\text{clr}}) = \lambda_1 E_{K(\text{clr})} + \lambda_2 E_{f(\text{tex})} + \int_\Omega |\nabla H(\phi)| \text{d}x\text{d}y, \tag{10}$$

where λ_1 and λ_2 are positive constants, $H(\cdot)$ is a Heaviside function and K_{clr} denotes prior color. The last term on the right of Eq. (10) is added to smooth contours [22].

2.2.3 Energy integration

To distinguish the relative importance of different energies, we need to solve the problem of parameter settings for λ_1 and λ_2, which decide which type of energy, prior color or texture plays a more important role in the MCMC sampling. Here, a novel method for setting λ_1 and λ_2 based on TL is proposed. TL is proposed here to describe the degree of texture complexity. Because texture reflects the changing patterns within a local range, color varies more greatly in more textured images. For an area with homogeneous color, texture generally has a very low level of complexity. In particular, TL is defined by:

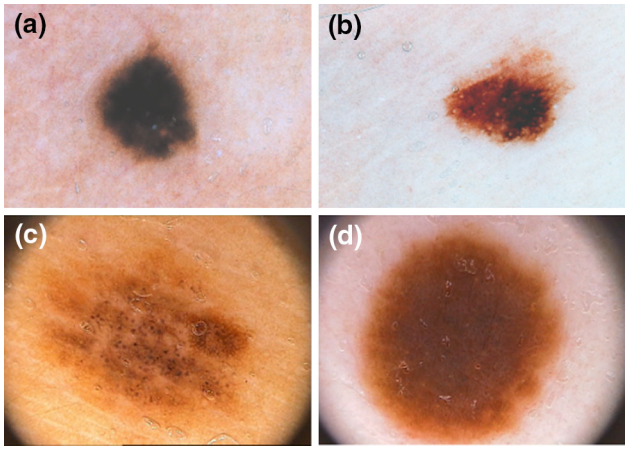

Fig. 5 Examples of different texture levels: **a** TL= 1.26, **b** TL= 2.23, **c** TL= 2.44 and **d** TL= 0.97

$$\text{TL} = -\sum_i p(r_i)\log_2(p(r_i)), \quad i = 1, 2, \ldots, L \tag{11}$$

where r_i is the ith color intensity level of the lesion area f_{Otsu} estimated by Otsu's method in the stage 1 of the proposed method, $p(r_i)$ denotes the histogram of the lesion area in terms of r_i and L is the maximum level of the discretization of lesion color. Here, if we set $L = 8$, then $\text{TL} \in [0,3]$. Some illustrative images with different TLs are shown in Fig. 5, where we can see that lesions with less color variation have smaller values of TL (see Fig. 5a, d) and that more color variation yields greater values of TL (Fig. 5b, c).

Based on the above analysis, λ_1 and λ_2 are set by

$$\lambda_1 = C,\ \lambda_2 = C \cdot \begin{cases} T_{\text{low}}, & \text{if } 0 \leq \text{TL} \leq 1, \\ T_{\text{med}}, & \text{if } 1 < \text{TL} \leq 2, \\ T_{\text{hgh}}, & \text{if } 2 < \text{TL} \leq 3, \end{cases} \tag{12}$$

where C is a positive constant and $T_{\text{hgh}} > T_{\text{med}} > T_{\text{low}} > 0$. The parameters are set in this way because texture features must play a more important role in segmentation if they are more obvious.

2.2.4 Global optimization based on MCMC sampling

After the energy functional based on level set is ready, the method of MCMC sampling in [24] is adopted here to find the global optimizers for the energy minimization

problem. Then, sufficient MCMC sampling will decrease the energy and generate an approximate globally optimal solution, which eventually defines a border in the image to segment a lesion from normal skin.

2.3 Postprocessing

After segmentation, mathematical morphology operations such as open, erode and close operators are used to fill in small holes inside lesions, smooth lesion borders and erase tiny islands apart from lesions. The disk-shaped structuring elements are used here, and the disk radius for open, erode and close operators is 2, 2 and 5, respectively.

3 Experiments

We use two public dermoscopy databases to test the segmentation algorithms. One database contains 90 images provided by Celebi et al. [37] and is called DB1. The other database is a challenging dermoscopic image database called PH^2, which includes 200 images that captured the complete region of skin lesions [38]. First, the numerical results are compared with those of 6 state-of-the-art algorithms. Then, the efficacy of applying texture level is analyzed.

Our experiments were conducted on a PC with a 2.5 GHz Intel Core2 Q8300 processor and 4 GB of 800 MHz DDR2 RAM running MATLAB 2013b on Windows XP. The default settings of the related parameters were as follows: Gabor wavelet scales = [0.1, 0.2, 0.5], $S = 3$; Gabor wavelet directions = [0, $\pi/4$, $\pi/2$, π*3/4], $K = 4$; $L = 8$; $C = 1$. For DB1, $n_1 = 0.8$, $T_{\text{low}} = 1\text{e}2$, $T_{\text{med}} = 1\text{e}7$ and $T_{\text{hgh}} = 1\text{e}9$; for PH^2, $n_1 = 2$, $T_{\text{low}} = 1\text{e}1$, $T_{\text{med}} = 1\text{e}3$ and $T_{\text{hgh}} = 1\text{e}8$.

3.1 Evaluation method

To evaluate the algorithms, segmentation results are compared with manually segmented ground truth, as determined manually by experienced dermatologists. For the numerical comparisons, we use the exclusive-OR (XOR) measure with respect to the correct classification of each pixel as normal skin or a lesion. Let TP be the number of true-positive pixels, FP the number of false positives, TN the number of true negatives and FN the number of false negatives. The formula for the metric is given in Eq. (13):

$$\text{XOR} = (\text{FP} + \text{FN})/(\text{TP} + \text{FN}). \tag{13}$$

3.2 Comparison with state-of-the-art algorithms

The proposed algorithm was first compared with 4 state-of-the-art lesion segmentation algorithms using DB1. These algorithms cover the major types of effective segmentation techniques.

Table 1 Comparison data of state-of-the-art algorithms for DB1 measured by XOR (%)

Algorithm	Benign		Melanoma		All	
	μ	σ	μ	σ	μ	σ
SRM [39]	11.38	6.23	**10.29**	5.84	11.11	6.12
ACE [31]	10.07	4.34	18.17	26.96	12.14	14.36
W30B60 [41]	12.95	6.17	16.93	7.16	13.96	6.63
DM [23]	**10.03**	4.34	13.11	4.88	10.82	4.66
SLS-CT	10.28	6.88	11.12	5.74	**10.50**	6.03

Table 1 lists the comparative results of performance measured by XOR, as defined in Eq. (13), using the DB1 database, where μ and σ are the mean value and the standard derivation of XOR, respectively. The best results are highlighted in boldface. The results show that the proposed algorithm has the smallest mean value of XOR for all images in DB1. The dataset is also divided into two categories: benign (67 images) and melanoma (23 images). Because benign lesions are always homogeneous in color, the results of XOR are satisfying ($\mu = 10.03$ to 13.69). Our algorithm is in the top 3, with $\mu = 10.28$ and $\sigma = 6.88$ for segmentation of benign lesions. Melanoma lesions are more textured than benign lesions, and the results for melanoma are consistent with this difference. Two algorithms presented $\mu > 15$ for melanoma segmentation. Our algorithm finished in second place, with $\mu = 11.12$ and $\sigma = 5.74$, while SRM [39] performed best, with $\mu = 10.29$ and $\sigma = 5.84$. The results of our algorithm are superior to those of similar methods for both benign and melanoma segmentation by distinguishing the relative importance of the two types of features based on TL.

Furthermore, the presented algorithm was compared with those proposed by Z. Ma and Tavares [23] and by Ahn et al. [40] using the PH^2 database. Notably, the algorithm presented in [23] used 160 of 200 images (8 for melanoma and 152 for nevi), thereby excluding most of the melanoma images, whereas we used 189 images in total (33 for melanoma and 156 for nevi), with many more challenging melanoma images. The algorithm in [40] used all 200 images.

Table 2 lists the comparative results measured by XOR using the PH^2 database from [23] and [40]. This table shows that the proposed algorithm yields the smallest mean values of XOR for both benign and all images in PH^2. For melanoma, however, SLS-CT has a larger value of XOR than that of the deformable model [23]. Note that our method used 33 melanoma images, while the compared algorithm used only 8. Moreover, the algorithm proposed by [23] is semiautomatic and requires manual initialization, whereas

Table 2 Comparison data of the algorithms for PH^2 measured by XOR (%)

Algorithm	Benign		Melanoma		All	
	μ	σ	μ	σ	μ	σ
DM [23]	13.91	7.79	**14.16**	8.07	13.92	7.78
RSSLS [40]	13.52	N/A	28.21	N/A	16.45	N/A
SLS-CT	**11.94**	8.29	19.80	8.19	**13.31**	8.64

Eleven images in PH^2 (IDs: IMD035, 037, 085, 168, 196, 240, 284, 367, 420, 424 and 425) are excluded from our experiments

our algorithm is fully automatic due to the usage of the novel index TL.

3.3 Efficacy of applying texture level

TL is introduced here to automatically decide the weight of each feature in the combined energy of the proposed model. Without TL, the weights are usually set manually and empirically. It is not only time-consuming but also hard to find optimal settings. The weight setting commonly accounts for the whole dataset but not for a single image. Setting weights per image is realizable with TL.

Figure 6 depicts the comparison of segmentation results between the algorithms with TL and without TL, measured by XOR, using boxplots. When setting weights manually, λ_1 is set to 1 constantly, and λ_2 is set to 14 different values as:

$$\lambda_2 \in \{1e-2, 1e-1, 1, 1e+1, 1e+2 \ldots, 1e+11\}.$$

In Fig. 6a, b, the rightmost boxplot of each figure is the result of the proposed method using TL, which outperforms the others without TL.

Additionally, when λ_2 is too small ($\lambda_2 = 1e-2$ or $1e-1$), i.e., the texture energy is nearly neglected, the performances are not satisfactory. With increasing values of λ_2, the values of XOR become significantly smaller (refer to the boxplots in Fig. 6 for $\lambda_2 = 1e-1, 1, 1e+1$). This further verified the validity of introducing texture in the combined energy. After that, the values of XOR fluctuate with the increase in λ_2. However, with the help of TL, λ_2 can be selected adaptively, and the resulting algorithm yields the best performance, as shown by the last boxplots in Fig. 6a, b.

3.4 Drawbacks and discussion

Our algorithm still failed to segment a small portion of images in PH^2. Two reasons may account for this: (1) some lesions are very similar to the surrounding normal skin in both color and texture and (2) some lesions have two or more different colors that are close to the background color. SLS-CT is not precise enough to discriminate between these lesions and the background. These cases can be found in the excluded images in PH^2 [30].

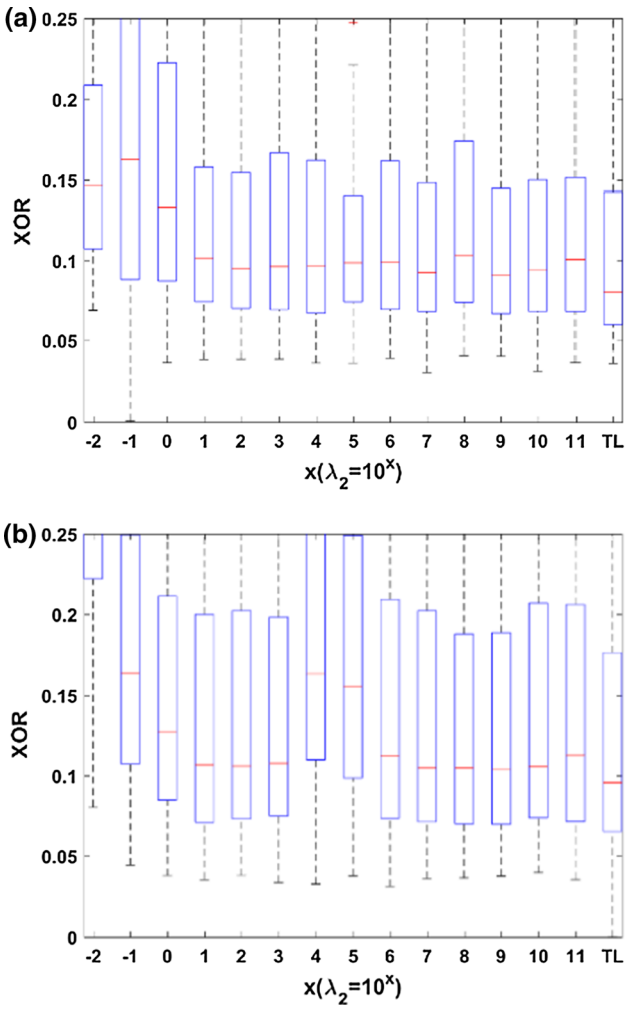

Fig. 6 The comparison of segmentation results between the algorithms with TL and without TL: **a** for DB1; **b** for PH^2

One possible way to solve these problems is to utilize the split-and-merge strategy in SLS-CT, i.e., first segmenting a dermoscopic image into more than two regions and then merging areas according to their regional features. This leaves us an open problem for future research.

4 Conclusions

SLS-CT, a novel pigmented skin lesion segmentation algorithm based on level set, is proposed. Based on TL, SLS-CT integrates adaptively the microfeatures of wavelet texture and prior color produced by Otsu thresholding into the energy functional and solves the problem of level set energy minimization by sampling based on MCMC to obtain global optimization. The proposed algorithm and other state-of-

the-art methods were tested and compared using two public dermoscopy databases. Numerical experimental results demonstrate the effectiveness and superiority of the proposed algorithm.

Acknowledgements This research was partly supported by the Guangdong Provincial Key Laboratory of Digital Signal and Image Processing Techniques (2013GDDSIPL-03), the Guangxi Natural Science Foundation (2018JJB170004), the Guangxi young and middle-aged teachers basic ability promotion project (2017KY0247), the Project of Cultivating a Thousand Young and Middle-aged Teachers in Guangxi Universities and the Guangxi Key Laboratory Fund of Embedded Technology and Intelligent System under Grant No. 2018A-07.

References

1. Celebi, M., Mendonca, T., Marques, J.: From dermoscopy to mobile teledermatology. In: Emre Celebi, M., Mendonca, T., Marques J.S. (eds.) Dermoscopy Image Analysis, pp. 385–418. CRC Press, Boca Raton (2015). https://www.taylorfrancis.com/books/9781482253269
2. Oliveira, R.B., Papa, J.P., Pereira, A.S., Tavares, J.M.R.S.: Computational methods for pigmented skin lesion classification in images: review and future trends. Neural Comput. Appl. **29**, 613–636 (2018)
3. Celebi, M.E., Iyatomi, H., Schaefer, G., Stoecker, W.V.: Lesion border detection in dermoscopy images. Comput. Med. Imaging Graph. **33**, 148–153 (2009)
4. Korotkov, K., Garcia, R.: Computerized analysis of pigmented skin lesions: a review. Artif. Intell. Med. **56**, 69–90 (2012)
5. Filho, M., Ma, Z., Tavares, J.M.: A review of the quantification and classification of pigmented skin lesions: from dedicated to hand-held devices. J. Med. Syst. **39**, 1–12 (2015)
6. Oliveira, R.B., Filho, M.E., Ma, Z., Pereira, A.S.: Computational methods for the image segmentation of pigmented skin lesions. Comput. Methods Progr. Biomed. **131**, 127–141 (2016)
7. Zhou, H., Schaefer, G., Sadka, A.H., Celebi, M.E.: Anisotropic mean shift based fuzzy C-means segmentation of dermoscopy images. IEEE J. Select. Top. Signal Process. **3**, 26–34 (2009)
8. Ashour, A.S., Hawas, A.R., Guo, Y., Wahba, M.A.: A novel optimized neutrosophic k-means using genetic algorithm for skin lesion detection in dermoscopy images. SIViP **12**, 1311–1318 (2018)
9. Dey, N., Rajinikanth, V., Ashour, A.S., Tavares, J.M.R.S.: Social group optimization supported segmentation and evaluation of skin melanoma images. Symmetry **10**, 51 (2018)
10. Oliveira, R.B., Marranghello, N., Pereira, A.S., Tavares, J.M.R.S.: A computational approach for detecting pigmented skin lesions in macroscopic images. Expert Syst Appl Int J **61**, 53–63 (2016)
11. Zhou, H., Li, X., Schaefer, G., Celebi, M.E., Miller, P.: Mean shift based gradient vector flow for image segmentation. Comput. Vis. Image Underst. **117**, 1004–1016 (2013)
12. Li, W., Li, F., Du, J.: A level set image segmentation method based on a cloud model as the priori contour. Signal Image Video Process. (2018). https://doi.org/10.1007/s11760-018-1334-5
13. Ma, Z., Tavares, J.M.R.S.: Effective features to classify skin lesions in dermoscopic images. Expert Syst. Appl. **84**, 92–101 (2017)
14. Oliveira, R.B., Pereira, A.S., Tavares, J.M.R.S.: Pattern recognition in macroscopic and dermoscopic images for skin lesion diagnosis. In: VipIMAGE 2017, Lecture Notes in Computational Vision and Biomechanics, vol. 27, pp. 504–514. Springer, Cham (2018)
15. Roth, H.R., Lu, L., Farag, A., Shin, H.C., Liu, J., Turkbey, E.B., Summers, R.M.: DeepOrgan: Multi-level deep convolutional networks for automated pancreas segmentation. In: Medical Image Computing and Computer-Assisted Intervention, vol. 9349, pp. 556–564. Munich (2015)
16. Hu, P., Yang, T.J.: Pigmented skin lesions detection using random forest and wavelet based texture. In: Proceeding of SPIE 10024, pp. 1X1–1X7 (2016)
17. Jafari, M.H., Nasresfahani, E., Karimi, N., Soroushmehr, S.M.R., Samavi, S., Najarian, K.: Extraction of skin lesions from non-dermoscopic images using deep learning. CoRR abs/1609.02374 (2016)
18. Kass, M., Witkin, A., Terzopoulos, D.: Snakes: active contour models. Int. J. Comput. Vis. **1**, 321–331 (1988)
19. Silveira, M., Nascimento, J.C., Marques, J.S., Marcal, A.R.S., Mendonca, T., Yamauchi, S., Maeda, J., Rozeira, J.: Comparison of segmentation methods for melanoma diagnosis in dermoscopy images. IEEE J. Selected Top. Signal Process. **3**, 35–45 (2009)
20. Erkol, B., Moss, R.H., Stanley, R.J., Stoecker, W.V., Hvatum, E.: Automatic lesion boundary detection in dermoscopy images using gradient vector flow snakes. Skin Res. Technol. **11**, 17–26 (2005)
21. Nascimento, J.C., Marques, J.S.: Adaptive snakes using the EM algorithm. IEEE Trans. Image Process. **14**, 1678–1686 (2005)
22. Chan, T.F., Vese, L.A.: Active contours without edges. IEEE Trans. Image Process. **10**, 266–277 (2001)
23. Ma, Z., Tavares, J.M.: A novel approach to segment skin lesions in dermoscopic images based on a deformable model. IEEE J. Biomed. Health Inf. **20**, 615–623 (2016)
24. Chang, J., Fisher, J.W.: Efficient MCMC sampling with implicit shape representations. In: IEEE Conference on Computer Vision and Pattern Recognition (CVPR), pp. 2081–2088. Providence (2011)
25. Oliveira, R.B., Pereira, A.S., Tavares, J.M.R.S.: Computational diagnosis of skin lesions from dermoscopic images using combined features. Neural Comput. Appl. (2018). https://doi.org/10.1007/s00521-018-3439-8
26. Celebi, M.E., Wen, Q., Iyatomi, H., Shimizu, K., Zhou, H., Schaefer, G.: A state-of-the-art survey on lesion border detection in dermoscopy images. In: Celebi, M.E., Mendonca, T., Marques, J.S. (eds.) Dermoscopy Image Analysis, pp. 97–129. CRC Press, Boca Raton (2015)
27. Celebi, M., Iyatomi, H., Schaefer, G., Stoecker, W.: Approximate lesion localization in dermoscopy images. Skin Res. Technol. **15**, 314–322 (2010)
28. Lee, T., Ng, V., Gallagher, R., Coldman, A., Mclean, D.: DullRazor: a software approach to hair removal from images. Comput. Biol. Med. **27**, 533–543 (1997)
29. Celebi, M.E., Kingravi, H.A., Vela, P.A.: A comparative study of efficient initialization methods for the k-means clustering algorithm. Expert Syst. Appl. **40**, 200–210 (2013)
30. Mokrzycki, W.S., Tatol, M.: Color difference Delta E—A survey. Mach. Graph. Vis. **20**, 383–411 (2011)
31. Schaefer, G., Rajab, M.I., Celebi, M.E., Iyatomi, H.: Colour and contrast enhancement for improved skin lesion segmentation. Comput. Med. Imaging Graph. **35**, 99–104 (2011)
32. Rother, C., Kolmogorov, V., Blake, A.: "GrabCut": interactive foreground extraction using iterated graph cuts. ACM Trans. Graph. **23**, 309–314 (2004)
33. An, N.-Y., Pun, C.-M.: Color image segmentation using adaptive color quantization and multiresolution texture characterization. SIViP **8**, 943–954 (2014)
34. Lee, T.S.: Image representation using 2D Gabor wavelet. IEEE Trans. Pattern Anal. Mach. Intell. **18**, 959–971 (2002)
35. Tsai, S.C., Tzeng, W.G., Wu, H.L.: On the Jensen–Shannon divergence and variational distance. IEEE Trans. Inform. Theory **51**, 3333–3336 (2005)
36. Baumgartner, J., Flesia, A.G., Gimenez, J., Pucheta, J.: A new image segmentation framework based on two-dimensional hidden Markov models. Integr. Comput. Aided Eng. **23**, 1–13 (2016)

37. Celebi, E.M., Quan, W., Sae, H., Hitoshi, I., Gerald, S.: Lesion border detection in dermoscopy images using ensembles of thresholding methods. Skin Res. Technol. **19**, e252–e258 (2013)
38. Mendonca, T., Ferreira, P.M., Marques, J.S., Marcal, A.R.S., Rozeira, J.: PH2—A dermoscopic image database for research and benchmarking. In: 35th Annual International Conference of the IEEE Engineering in Medicine and Biology Society, pp. 5437–5440 (2013). http://www.fc.up.pt/addi/ph2%20database.html
39. Celebi, M., Kingravi, H., Aslandogan, Y., Stoecker, W., Moss, R., Malters, J., Grichnik, J., Marghoob, A., Rabinovitz, H., Menzies, S.: Border detection in dermoscopy images using statistical region merging. Skin Res. Technol. **14**, 347–353 (2008)
40. Ahn, E., Kim, J., Bi, L., Kumar, A., Li, C., Fulham, M., Feng, D.D.: Saliency-based lesion segmentation via background detection in dermoscopic images. IEEE J. Biomed. Health Inf. **21**, 1685–1693 (2017)
41. Garnavi, R., Aldeen, M., Celebi, M.E., Varigos, G., Finch, S.: Border detection in dermoscopy images using hybrid thresholding on optimized color channels. Comput. Med. Imaging Graph. **35**, 105–115 (2011)